

DOUBLE COMPACT OBJECTS III: GRAVITATIONAL-WAVE DETECTION RATES

MICHAŁ DOMINI¹, EMANUELE BERTI², RICHARD O'SHAUGHNESSY³, ILYA MANDEL⁴, KRZYSZTOF BELCZYŃSKI^{1,5},
CHRISTOPHER FRYER⁶, DANIEL E. HOLZ⁷, TOMASZ BULIK¹, FRANCESCO PANNARALE⁸

¹ Astronomical Observatory, University of Warsaw, Al. Ujazdowskie 4, 00-478 Warsaw, Poland

² Department of Physics and Astronomy, The University of Mississippi, University, MS 38677, USA

³ Center for Gravitation, Cosmology, and Astrophysics, University of Wisconsin-Milwaukee, Milwaukee, WI

⁴ School of Physics and Astronomy, University of Birmingham, Edgbaston, Birmingham B15 2TT, United Kingdom

⁵ Center for Gravitational Wave Astronomy, University of Texas at Brownsville, Brownsville, TX 78520

⁶ CCS-2, MSD409, Los Alamos National Laboratory, Los Alamos, NM 87545

⁷ Enrico Fermi Institute, Department of Physics, and Kavli Institute for Cosmological Physics
University of Chicago, Chicago, IL 60637

⁸ School of Physics and Astronomy, Cardiff University, The Parade, Cardiff CF24 3AA, United Kingdom

Draft version December 6, 2024

ABSTRACT

The unprecedented range of second-generation gravitational-wave (GW) observatories calls for refining the predictions of potential sources and detection rates. The coalescence of double compact objects (DCOs)—i.e., neutron star-neutron star (NS-NS), black hole-neutron star (BH-NS), and black hole-black hole (BH-BH) binary systems—is the most promising source of GWs for these detectors. We compute detection rates of coalescing DCOs in second-generation GW detectors using the latest models for their cosmological evolution, and implementing inspiral-merger-ringdown (IMR) gravitational waveform models in our signal-to-noise ratio calculations. We find that: (1) the inclusion of the merger/ringdown portion of the signal does not significantly affect rates for NS-NS and BH-NS systems, but it boosts rates by a factor ~ 1.5 for BH-BH systems; (2) in almost all of our models BH-BH systems yield by far the largest rates, followed by NS-NS and BH-NS systems, respectively, and (3) a majority of the detectable BH-BH systems were formed in the early Universe in low-metallicity environments. We make predictions for the distributions of detected binaries and discuss what the first GW detections will teach us about the astrophysics underlying binary formation and evolution.

Subject headings: double compact objects, merger rates, cosmology

1. INTRODUCTION

Nearly a century has passed since Albert Einstein wrote down the field equations of general relativity. A crucial prediction of his theory is the existence of GWs. Observations of the Hulse-Taylor binary pulsar (Taylor & Weisberg 1989) and the double pulsar J0737-3039 (Lyne et al. 2004) leave little doubt of the existence of GWs, with further evidence provided by the recent claim of a detection of a GW-induced B-mode polarization of the cosmic microwave background (BICEP2 Collaboration et al. 2014). However, GWs still elude direct observation. The situation should change in the next few years, when a network of second-generation GW observatories – including Advanced LIGO (Harry, 2010, henceforth aLIGO), Advanced Virgo (Virgo Collaboration 2009, henceforth AdV), and KAGRA (Somiya 2012) – will start taking data. The unprecedented sensitivity of these observatories will allow them to observe the inspiral and merger of DCOs out to cosmological distances: for example, aLIGO should observe binary neutron stars out to a luminosity distance of $\simeq 450$ Mpc ($z \sim 0.1$), while DCOs containing BHs will be observable to much larger distances (e.g., Abadie et al. 2010). Given the cosmological reach of second-generation GW interferometers, a theoretical investigation of the observable DCO populations which incorporates cosmological evolution and accurate models of the gravitational waveforms is particularly timely. This is the goal of this paper, the

third in a series (cf. Dominik et al. 2012, 2013). Our work builds on the results presented in the second paper (Dominik et al. 2013, henceforth Paper 2), where we presented the cosmological distribution of DCOs for a set of four evolutionary models. These models investigated a range of Hertzsprung gap (HG) common envelope (CE) donors, supernova (SN) explosion engines, and BH natal kicks, showing distinct differences in the properties of the resulting DCO populations. Population models were placed in a cosmological context by adopting the star formation history reported in Strolger et al. (2004) and the galaxy mass distribution of Fontana et al. (2006), both of which are redshift-dependent. We performed all calculations assuming two scenarios for metallicity evolution, meant to bracket the uncertainties associated with the chemical composition of the Universe. Binary evolution was performed using the **StarTrack** population synthesis code (Belczynski et al. 2008).

In this work we complete and extend the analysis of Paper 2. We study the detection rates and the expected physical properties of coalescing DCOs at cosmological distances for second-generation GW observatories. The rates are calculated for different sets of gravitational waveform models and different detector sensitivities, representative of aLIGO, AdV, and KAGRA. Several different groups have presented similar estimates and studies in the past decade (e.g., Grishchuk et al. 2001; Nelemans et al. 2001; Voss & Tauris 2003a; Dewi & Pols 2003; Nutzman et al.

2004; Pfahl et al. 2005; De Donder & Vanbeveren 2004; Postnov & Yungelson 2006). However, none have combined cosmological DCO populations with accurate GW models to obtain thorough, detector-specific results. Our astrophysical models for DCO formation are reviewed in Section 2. Gravitational waveform models and signal-to-noise ratio estimates are discussed in Section 3. Our procedure to compute event rates is presented in Section 4. Event rates and bulk properties of the detected populations are presented in Section 5. In Section 6 we discuss the possible astrophysical payoff of the first GW detections and important directions for future work.

2. ASTROPHYSICAL MODELS

2.1. Binary evolution

We begin with a summary of the four **StarTrack** evolutionary models that form the backbone of this work; a more detailed discussion can be found in Dominik et al. (2012, 2013).

1) *Standard model*. This is our reference model, representing the state of the art in the formation and evolution of binary systems. We consider only field populations here. Rate estimates performed for dense populations in which dynamical interactions between stars are important (i.e., globular clusters) have been presented elsewhere (Gültekin et al. 2004; O’Leary et al. 2006; Grindlay et al. 2006; Sadowski et al. 2008; Ivanova et al. 2008; Downing et al. 2010; Miller & Lauburg 2009). Our Standard model uses the “Nanjing” (Xu & Li 2010) λ coefficient in the CE energy balance prescription of Webbink (1984), where the precise value of λ depends on the evolutionary stage of the donor, its Zero Age Main Sequence (ZAMS) mass, the mass of its envelope, and its radius. In turn, these quantities depend on metallicity, which in our simulations varies within the broad range $10^{-4} \leq Z \leq 0.03$ (recall that solar metallicity corresponds to $Z_{\odot} = 0.02$). The values of λ for high-mass stars ($M_{ZAMS} > 20 M_{\odot}$) were obtained through private communication with the authors and are not present in Xu & Li (2010).

The impact of the CE outcome on binary populations depends strongly on the evolutionary stage of the donor, as first discussed in Belczynski et al. (2007). The Standard model does not allow for CE events with HG donors. These stars are not expected to possess a clear core-envelope structure (Ivanova & Taam 2004), thus making it difficult for them to eject their outer layers during the CE phase. In our Standard model all CE events with HG donors lead to a prompt merger before a DCO binary is formed, regardless of the aforementioned energy balance.

The model employs a Maxwellian distribution of natal kicks for NSs with 1-D root mean square velocity $\sigma = 265$ km/s, consistent with NS observations (Hobbs et al. 2005). The same distribution is extended to BHs, where we allow for the possibility that the kicks may be reduced due to fallback of material during the SN that leads to BH formation. The reduction in BH kicks is described via

$$V_k = V_{\max}(1 - f_{\text{fb}}), \quad (1)$$

where V_k is the final magnitude of the natal kick, V_{\max} is the velocity drawn from a Maxwellian kick distribution, and f_{fb} is a “fallback factor” that depends on the amount

of fallback material, calculated according to the prescription given in Fryer et al. (2012a). Our Standard model uses the “Rapid” convection-driven, neutrino-enhanced SN engine (Fryer et al. 2012a). The SN explosion is sourced from the Rayleigh-Taylor instability and occurs within the first 0.1–0.2 s. When used in the context of binary evolution models, this SN engine successfully reproduces the mass gap (Belczynski et al. 2012c) observed in Galactic X-ray binaries (Bailyn et al. 1998; Özel et al. 2010), but see also Kreidberg et al. (2012).

2) *Optimistic Common Envelope*. In this model we allow HG stars to be CE donors. When the donor initiates the CE phase, the CE outcome is determined via energy balance. The remaining physics is identical to the Standard model.

3) *Delayed SN*. This model utilizes the “Delayed” SN engine instead of the Rapid one. The former is also a convection driven, neutrino enhanced engine, but is sourced from the standing accretion shock instability (SASI), and can produce an explosion as late as 1 s after bounce. The Delayed engine produces a continuous mass spectrum of compact objects, ranging from NSs through light BHs to massive BHs (Belczynski et al. 2012c).

4) *High BH kicks*. In this model the BHs receive full natal kicks, i.e. we set $f_{\text{fb}} = 0$ in Eq. (1). Otherwise this model is identical to the Standard model.

2.2. Metallicity evolution

In this paper we employ two distinct metallicity evolution scenarios: “high-end” and “low-end”. These are identical to those in our previous study (Paper 2), and a detailed description can be found therein. Employing such calibrations allows us to explore and bracket uncertainties in the chemical evolution of the Universe. In both cases the average metallicity decreases with increasing redshift.

The high-end metallicity profile is calibrated to yield a median value of metallicity equal to $1.5 Z_{\odot}$ (or 8.9 in the “ $12+\log(\text{O}/\text{H})$ ” formalism) at redshift $z = 0$. This calibration was designed to match the upper 1σ scatter of metallicities according to Yuan et al. (2013) (see their Fig. 2, top-right panel).

The low-end metallicity profile is based on SDSS observations (Panter et al. 2008), from which we infer that one half of the star forming mass of galaxies at $z \sim 0$ has 20% solar metallicity, while the other half has 150% solar metallicity.

3. WAVEFORM MODELS

3.1. Order-of-magnitude estimates

For any given GW detector the “horizon distance”, D_h , is defined as the luminosity distance at which an optimally oriented canonical $(1.4 + 1.4) M_{\odot}$ NS-NS binary would be detected at a fiducial threshold signal-to-noise ratio (SNR), taken to be 8 in this paper. The expectation value of the SNR, ρ , of a signal with GW amplitude $h(t)$ is given by

$$\rho^2 = 4 \int_0^{\infty} \frac{|\tilde{h}(f)|^2}{S_n(f)} df, \quad (2)$$

TABLE 1
LOCAL MERGER RATES AND SIMPLY-SCALED DETECTION RATE PREDICTIONS^a:

Model	$\langle \mathcal{M}_c^{15/6} \rangle$ $M_\odot^{15/6}$	$\mathcal{R}(0)$ $\text{Gpc}^{-3} \text{yr}^{-1}$	R_D (aLIGO $\rho \geq 8$) yr^{-1}	R_D (3-det network $\rho \geq 10$) yr^{-1}
NS-NS				
Standard	1.1 (1.1)	61 (52)	1.3 (1.1)	3.2 (2.7)
Optimistic CE	1.2 (1.2)	162 (137)	3.9 (3.3)	9.2 (7.7)
Delayed SN	1.4 (1.4)	67 (60)	1.9 (1.7)	4.5 (4.0)
High BH Kicks	1.1 (1.1)	57 (52)	1.2 (1.1)	3.0 (2.7)
BH-NS				
Standard	18 (19)	2.8 (3.0)	1.0 (1.2)	2.4 (2.7)
Optimistic CE	17 (16)	17 (20)	5.7 (6.5)	13.8 (15.4)
Delayed SN	24 (20)	1.0 (2.4)	0.5 (0.9)	1.1 (2.3)
High BH Kicks	19 (13)	0.04 (0.3)	0.01 (0.08)	0.04 (0.2)
BH-BH				
Standard	402 (595)	28 (36)	227 (427)	540 (1017)
Optimistic CE	311 (359)	109 (221)	676 (1585)	1610 (3773)
Delayed SN	829 (814)	14 (24)	232 (394)	552 (938)
High Kick	2159 (3413)	0.5 (0.5)	22 (34)	51 (81)

^a Detection rates computed using the basic scaling of Eq. (3) for both the *high-end* and *low-end* (the latter in parentheses) metallicity scenarios (see Section 2.2). These rates should be compared with those from more careful calculations presented in Tables 2 and 3.

where $\tilde{h}(f)$ is the Fourier transform of the signal and $S_n(f)$ is the noise power spectral density of the detector (see e.g. Cutler & Flanagan 1994; Poisson & Will 1995). The square root of the noise power spectral density is plotted in Fig. 1 for several advanced interferometers of interest. For example, the aLIGO horizon distance is $D_h \simeq 450$ Mpc.

Although the sensitivity of a GW detector network depends on the details of the search pipeline and the detector data quality, we follow Abadie et al. (2010) in considering a single detector with an SNR threshold $\rho \geq 8$ as a proxy for detectability by the network. With this criterion, a simple and common expression to transform the local merger rate to a predicted detection rate R_D , given the horizon distance D_h and the merger rate density, $\mathcal{R}(z)$, evaluated locally (at $z = 0$), is:

$$R_D \simeq \frac{4\pi}{3} D_h^3 \langle w^3 \rangle \langle (\mathcal{M}_c / 1.2 M_\odot)^{15/6} \rangle \mathcal{R}(0) \quad (3)$$

In this expression $\langle w^3 \rangle^{-1/3} \simeq 2.264$ is a purely geometrical and SNR-threshold-independent factor commonly used to relate sky location- and orientation-averaged distances to optimal detection distances (see Appendix for details) and $\mathcal{M}_c = \eta^{3/5} M$ (where $M = m_1 + m_2$ is the total mass of the binary and $\eta \equiv m_1 m_2 / M^2$) is the “chirp mass” (see, e.g., Cutler & Flanagan 1994). This estimate assumes that (1) cosmological effects are negligible (i.e., space is Euclidean to a good approximation), and (2) most of the SNR is accumulated during an inspiral phase which lasts through the entire sensitive band of the detector, where the GW amplitude in the frequency domain is well approximated by the quadrupole formula, i.e., $\tilde{h}(f) \sim \mathcal{M}_c^{5/6} f^{-7/6} / D$. Here D is the luminosity distance to the source. The estimate of Eq. (3) follows from this simple scaling together with the definition of the SNR, Eq. (2).

Eq. (3) involves only the *local* merger rate $\mathcal{R}(0)$ and $\langle \mathcal{M}_c^{15/6} \rangle$ is averaged over detected binaries. Both quantities can easily be extracted from **StarTrack** simulations; they are listed in Table 1, along with the values of R_D predicted by Eq. (3). We expect this rough esti-

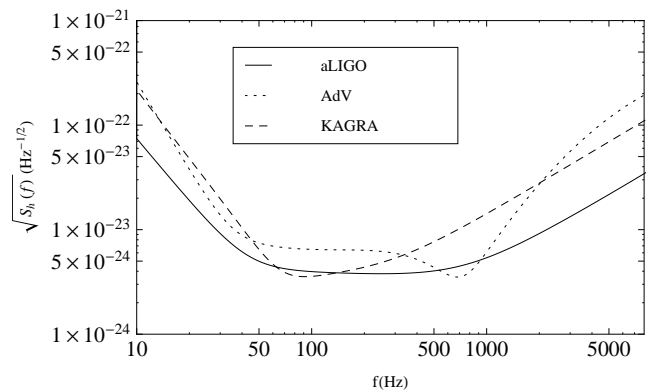


FIG. 1.— **Noise models:** we use an analytical approximation to the aLIGO zero-detuning high power (ZDHP) noise power spectral density given in Eq. (4.7) of Ajith (2011) (we verified that this approximation gives results in excellent agreement with the “official” tabulated aLIGO ZDHP noise PSD given in Shoemaker, D. for the LIGO Scientific Collaboration (2010). For AdV we use the fit in Eq. (3.4) of Ajith & Bose (2009) to Virgo Collaboration (2009), and for KAGRA we use the PSD fit from the Appendix of Pannarale et al. (2013) to Somiya (2012).

mate to be accurate for NS-NS binaries, for which the overwhelming majority of the SNR is accumulated during the inspiral phase. More accurate calculations are required for DCOs comprised of BHs, because they are visible out to larger distances (making cosmological corrections important) and because, as we discuss below, a large fraction of the SNR for these binaries comes from the merger/ringdown portion of the signal.

3.2. Including merger and ringdown

In order to refine our rate estimates for high-mass systems containing BHs, it is important to consider the full waveform, including inspiral, merger, and ringdown. The calculation of gravitational waveforms from merging BH-BH and BH-NS binaries requires expensive numerical relativity simulations, but several semi-analytical models have been tuned to reproduce the amplitude and phasing of BH-BH and BH-NS merger simulations. To estimate systematic uncertainties and the impact of spin,

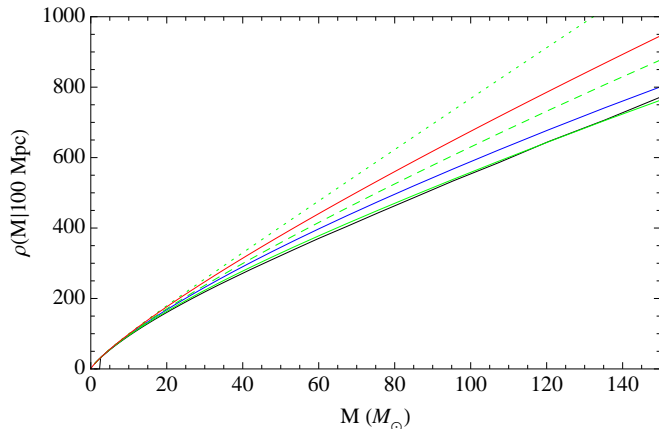


FIG. 2.— **SNR for different signal models:** To illustrate the relatively small differences between the signal models we have adopted, we show the SNR, $\rho(M)$, as a function of total binary mass, M , for an equal-mass nonspinning binary at 100 Mpc, where the SNR is evaluated using a single fiducial aLIGO detector. The colored solid curves show (a) the trivial expression $\rho = \rho_0 (M/2.8M_\odot)^{5/6}$ with $\rho_0 = 34.3$ (red), (b) an EOB model (black), PhB model (blue), and PhC model (green), all evaluated for zero spin. The green dotted line shows the PhC model evaluated with near-extremal spin on both objects ($\chi_1 = \chi_2 = 0.998$), while the green dashed line shows PhC with near-extremal spin on one object ($\chi_1 = 0.998, \chi_2 = 0$). The choice $\chi_i = 0.998$ corresponds to the Thorne (1974) bound. This value of the spin is outside the regime in which phenomenological models have been calibrated, and it has been chosen to provide rough upper limits on the rates.

we performed rate calculations using three models: (1) the IMRPhenomB model described in Ajith et al. (2011), one of the earliest phenomenological models tuned to both nonspinning and spinning BH-BH simulations with aligned spins, henceforth abbreviated as PhB; (2) the IMRPhenomC (henceforth abbreviated PhC) model by Santamaría et al. (2010), a more accurate alternative to PhB also tuned to nonprecessing simulations of BH-BH mergers; and (3) a nonspinning effective-one-body (EOB) model (Pan et al. 2010). A detailed comparison of the three models can be found in Damour et al. (2011). Recent work by Pannarale et al. (2013) shows that finite-size effects introduce negligible errors ($\lesssim 1\%$) in SNR calculations for BH-NS binaries, therefore the above models are adequate for *both* BH-BH and BH-NS binaries. In order to facilitate comparison with previous work, we also evaluated rates using the simplest possible approximation: a restricted post-Newtonian (PN) waveform where the amplitude is truncated at Newtonian order, i.e. $\tilde{h}(f) \sim \mathcal{M}_c^{5/6} f^{-7/6} / D$, terminated at a fiducial “innermost stable circular orbit” frequency $f_{\text{ISCO}} = (GM\pi/c^3)^{-1} 6^{-3/2}$. At low mass, the upper limit can be neglected and this approximation corresponds to $\rho \propto \mathcal{M}_c^{5/6}$, as stated above: see also Eq. (7) in O’Shaughnessy et al. (2010a).

Figure 2 shows that these models all make similar predictions for the SNR of optimally oriented equal-mass binaries as a function of their total mass for a single aLIGO detector. Even small differences can be important: for any given binary, a 30% difference in amplitude corresponds to a factor $(1.3)^3 \simeq 2.2$ in rate calculations. In practice, however, all nonspinning IMR models agree in SNR to within tens of percent over the total binary mass range of interest (up to 127 M_\odot , see Section 5.3). The ef-

fect of spin will be discussed in more detail in Section 5.2 below.

Figure 3 shows contour plots of the SNR, ρ , in the (M_z, q) plane, where $M_z \equiv M(1+z)$ is the redshifted total mass, z is the redshift, and $q = m_1/m_2 \leq 1$ is the mass ratio of the components, for nonspinning binaries at luminosity distance $D_L = 100$ Mpc. We discuss the justification for considering the SNR as a function of M_z below, but since the chosen distance corresponds to a negligible redshift $z \simeq 0.023$ using the cosmological parameters $\Omega_M = 0.3$, $\Omega_\Lambda = 0.7$, $\Omega_k = 0$, and $h = 0.7$ (chosen for consistency with Dominik et al. (2012, 2013)), $M \simeq M_z$ at this distance. The left panel refers to a calculation using an inspiral-only waveform with Newtonian amplitude to compute the horizon distance. The right panel includes inspiral, merger, and ringdown, modelled using the PhC waveform. This plot shows two important features: (1) including the full IMR increases the maximum SNR at this luminosity distance by factors of a few with respect to an inspiral-only calculation, from ≈ 300 to $\approx 10^3$; (2) high-mass binaries ($M_z \gtrsim 10^{2.5} M_\odot \approx 300 M_\odot$) involving BHs that would not be detectable using inspiral waveforms, become detectable using IMR waveforms. The latter point is not important for the field binaries considered in this paper, but it is crucial for intermediate-mass BH mergers (e.g., Belczynski et al. 2014; Fregeau et al. 2006; Amaro-Seoane & Freitag 2006).

In an expanding Universe, GW emission is redshifted by the same factor of $(1+z)$ as electromagnetic radiation. The parameter setting the timescale for the evolution of a black-hole binary is the binary’s total mass, M . Therefore, a binary source of mass M in the local universe has an identical waveform (but with different amplitude) to a binary at redshift z with mass $M/(1+z)$; see, e.g., Flanagan & Hughes (1998). Eq. (2), together with the fact that gravitational amplitudes scale inversely with the luminosity distance $D_L(z)$, implies that the horizon redshift z_h (i.e., the redshift at which an optimally located and oriented binary would have SNR $\rho_{\text{thr}} = 8$) can be found via the simple scaling

$$D_h(z_h) = D_L(z) \frac{\rho(M_z, q)}{\rho_{\text{thr}}}, \quad (4)$$

where ρ is the SNR at any redshift z , or luminosity distance $D_L(z)$. Note that the right-hand side depends only on z , M_z and q . Therefore one can easily turn an SNR calculation at fixed z (cf. Fig. 3) into a plot of the horizon luminosity distance D_h (or equivalently of the horizon redshift z_h) such as Fig. 4.

StarTrack produces large catalogs of DCOs with intrinsic parameters (M, q) , with each of these binaries merging at a different redshift. Any of these representative DCOs is potentially detectable (depending on precise sky location and binary orientation) when $z < z_h$. Determining detectability therefore amounts to a simple interpolation of two-dimensional grids similar to those plotted in Fig. 4. These grids can be computed once and for all, given a waveform model and a detector’s power spectral density (PSD). Evaluating such a grid typically involves $100 \times 100 = 10^4$ SNR evaluations, and it is much faster than the (impractical) evaluation of millions of SNR integrals such as Eq. (2), one for each representative bi-

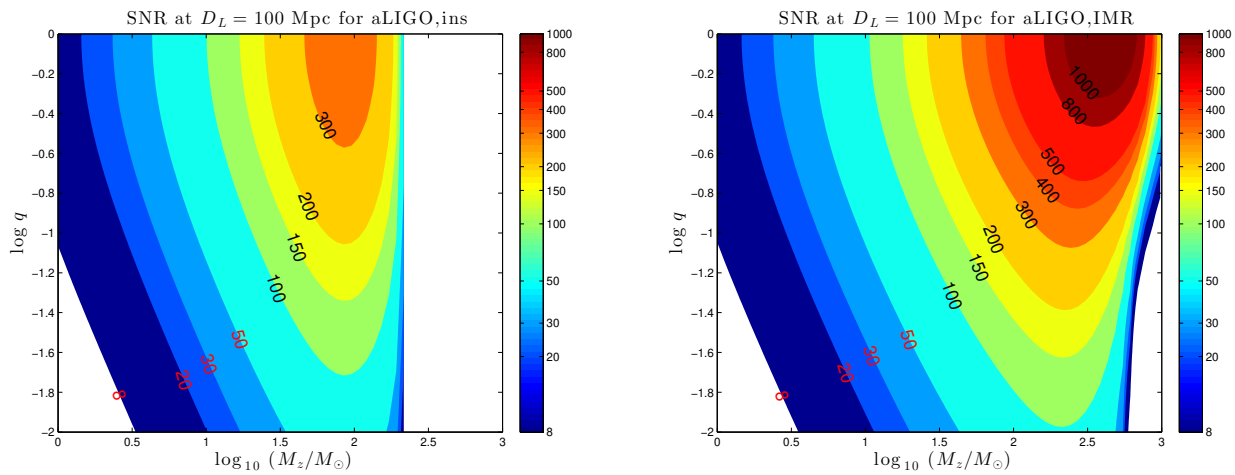


FIG. 3.— **Optimal SNR for nonspinning binaries** of given (redshifted) total mass $M_z = M(1+z)$ and mass ratio $q = m_2/m_1$ at luminosity distance $D_L = 100$ Mpc. In the left panel the SNR is computed using the restricted PN approximation (i.e., the GW amplitude is evaluated using the quadrupole formula). In the right panel we use the PhC model for the full IMR waveform; the results for the EO model are very similar. A low-frequency cutoff of $f_{\text{cut}} = 20$ Hz has been assumed (see Section 5.2 for further details).

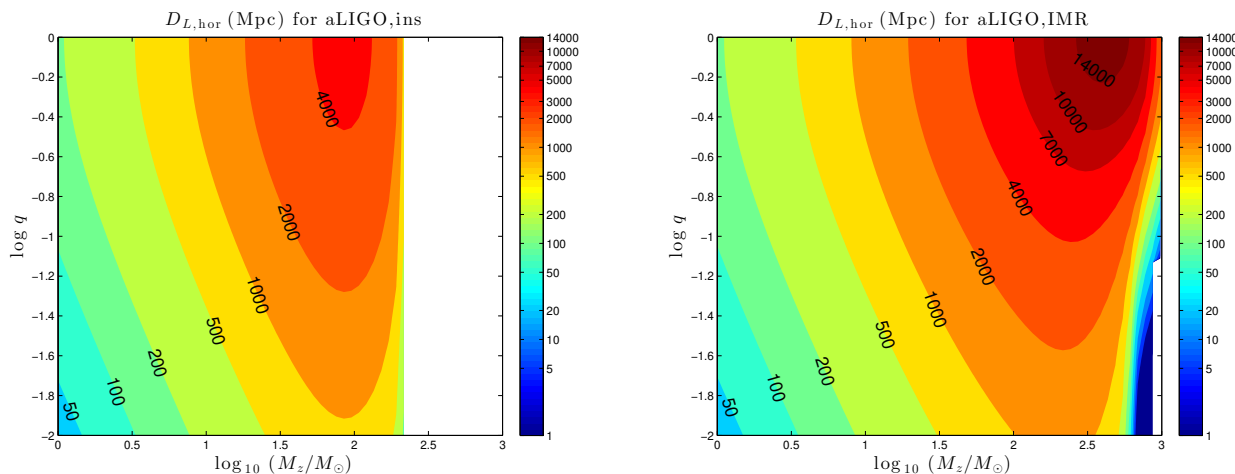


FIG. 4.— **Horizon luminosity distance (in Mpc) for nonspinning binaries** as a function of redshifted mass and mass ratio, computed according to Eq. (4) using waveforms comprised of only the inspiral (left panel) or the full IMR signal (right panel).

binary produced by StarTrack. The conversion between detectability at optimal location and optimal orientation and detectability at generic orientations involves a simple geometrical factor p_{det} , as discussed below.

4. RATE CALCULATION

The detection rate is

$$R_{\text{det}} = \iiint \mathcal{R}(z_m) \frac{dt_m}{dt_{\text{det}}} p_{\text{det}} \frac{dV_c}{dz_m} dz_m dm_1 dm_2, \quad (5)$$

where $\mathcal{R}(z_m) \equiv \frac{dN}{dm_1 dm_2 dV_c dt_m}$ is the binary merger rate per unit comoving volume V_c per unit time t_m as measured in the source frame at merger redshift z_m , the term $\frac{dt_m}{dt_{\text{det}}} = \frac{1}{1+z_m}$ accounts for the difference in clock rates at the merger and at the detector, and $p_{\text{det}} = p_{\text{det}}(z_m; m_1, m_2)$ is the probability (over isotropic sky locations and orientations) that a source with given masses at a given redshift will be

detectable. The quantity

$$\frac{dV_c}{dz} = \frac{4\pi c}{H_0} \frac{D_c^2(z)}{E(z)}, \quad (6)$$

with $E(z) = \sqrt{\Omega_M(1+z)^3 + \Omega_k(1+z)^2 + \Omega_\Lambda}$, is the comoving volume per unit redshift, and

$$D_c(z) = \frac{c}{H_0} \int_0^z \frac{dz'}{E(z')} \quad (7)$$

is the comoving distance, related to the luminosity distance $D_L(z)$ by $D_c(z) = D_L(z)/(1+z)$: see Hogg (1999) for our notation and conventions.

The merger rate $\mathcal{R}(z_m)$ is a convolution of the star formation rate and the number density of binaries per unit star forming mass M_f per unit time delay between

formation and merger τ :

$$\mathcal{R}(z_m) = \int_0^{t_m} \int_0^{t_{\text{det}}} \frac{dM_f}{dV_c dt_f}(z_f) \frac{dN}{dM_f dm_1 dm_2 d\tau}(t_f; m_1, m_2, \tau) \times \delta(t_m - t_f - \tau) d\tau dt_f, \quad (8)$$

where $\text{SFR} = \frac{dM_f}{dV_c dt_f}(z_f)$ is the star formation rate per unit comoving volume per unit time t_f at formation redshift z_f .

The distribution of binaries in mass and time delay space, $\frac{dN}{dM_f dm_1 dm_2 d\tau}(t_f; m_1, m_2, \tau)$, is obtained with the **StarTrack** population synthesis code, taking into account the metallicity distribution at the formation redshift as described in Section 2. Since **StarTrack** simulations produce a set of merging binaries with specific component masses and time delays sampling the desired distribution, the integrals above are easily computed via Monte Carlo over the simulated systems. For computational efficiency the outer integral over the time of formation in Eq. (8) is binned over $\Delta t_f = 100$ Myr segments, while the integral over the merger redshift z_m in Eq. (5) is transformed into an integral over merger time via $dz_m = \frac{dz_m}{dt_m} dt_m = H_0(1+z)E(z)dt_m$ (Hogg 1999). Thus the detection rate integral can be represented as a Monte Carlo sum over all simulated binaries:

$$R_{\text{det}} = \sum \frac{\text{SFR}}{\Delta M_f} p_{\text{det}} \frac{1}{1+z} \frac{dV_c}{dz} \frac{dz}{dt} \Delta t, \quad (9)$$

where ΔM_f is the total star-forming mass that was simulated in the Monte Carlo to represent the time bin Δt , all terms but the first are computed at the merger redshift of the simulated source.

The detection probability for a given source at its merger redshift $p_{\text{det}}(z, m_1, m_2)$ is simply the fraction of sources of a given mass located at the given redshift that exceed the detectability threshold in SNR, assuming that sources are uniformly distributed in sky location and orbital orientation. If a single detector with an SNR threshold (e.g., $\rho_{\text{thr}} = 8$) is used as a proxy for detectability, the detection probability can be expressed as a cumulative distribution function on the projection parameter w . In the Appendix, w is defined such that $w = 0$ when the detector has no response to the gravitational wave, and $w = 1$ for an optimally located and oriented (face-on and directly overhead) binary. The detection probability is

$$p_{\text{det}} = P(\rho_{\text{thr}}/\rho_{\text{opt}}), \quad (10)$$

where $P(w)$ is the cumulative distribution function on w over different source locations and orientations, and ρ_{opt} is the signal-to-noise ratio (SNR) for an optimally located and oriented binary at redshift z .

5. RESULTS

In Section 3.1 we obtained a rough estimate of event rates by extrapolating the local rate density via the scaling of Eq. (3). This extrapolation is expected to provide a good approximation for low-mass systems (and in particular, NS-NS binaries), because in this case the early inspiral makes up most of the signal observable by advanced GW detectors, the signal extends through the detector band, and the detector range is sufficiently low

that cosmological corrections to detectability and the dependence of merger rates on redshift can largely be ignored. The approximation will become increasingly inaccurate for high-mass binaries, such as those comprising one or two BHs. In Sections 3.2 and 4 we went beyond this approximation by implementing three “complete” IMR waveform models (EOB, PhC, PhB), and we described how to combine these models with simulations from the **StarTrack** code in order to obtain more accurate estimates of the event rates (see Eq. (9)).

The analytical estimates of Section 3.1 with local merger rates based on the **StarTrack** code are presented in Table 1. The more careful event rate calculations of Section 4 are listed in Table 2 (for the high-end metallicity scenario) and Table 3 (for the low-end metallicity scenario).

In these tables, the “single-detector” columns represent estimated detection rates for a single detector with a $\rho \geq 8$ threshold for detectability. This is often used as a proxy for rates in multi-detector networks (Abadie et al. 2010). In the “three-detector” columns we consider two alternate detectability thresholds: minimum *network* SNRs of either 10 or 12 for a three-detector network composed of three instruments located at the LIGO Hanford, LIGO Livingston, and Virgo sites, all with aLIGO sensitivity. The network SNR threshold of 10 would have yielded false alarm rates of roughly once per decade in 2009-2010 initial LIGO and Virgo data (see Fig. 3 in Aasi et al. 2013b). This threshold is optimistic for making confident detections if data quality in advanced detectors is similar to that in the initial detectors and the same searches are used. With this in mind, Aasi et al. (2013b) assumed a network SNR threshold of 12 with an additional threshold constraint on the SNR in the second-loudest instrument; we consider a simple SNR threshold of 12. Detection rates using a network SNR threshold were calculated using the same framework as above, but implementing a network-geometry-dependent $P(w)$ described (and fitted) in the Appendix. In the order-of-magnitude estimates described by Eq. (3) and provided in Table 1 we employ $\langle w^3 \rangle \simeq 0.404$ for the three-detector network ($\rho \geq 10$), a factor of ~ 4.6 larger than the value $\langle w^3 \rangle \simeq (1/2.26)^3 \approx 0.0866$ used for a one-detector network.

We now discuss these rate predictions, their dependence on gravitational waveform models, and the astrophysical properties of DCO populations observable by advanced GW detectors.

5.1. Broad features of rate estimates

The main conclusion of this work is that BH-BH mergers should yield the highest detection rates in all advanced detectors (aLIGO, AdV, and KAGRA), followed by NS-NS mergers, with BH-NS mergers being the rarest. This finding is independent of the evolutionary model and of the details of the gravitational waveform. The only exception is the “Optimistic CE” model, where detection rates for BH-NS mergers dominate over NS-NS mergers (with BH-BH mergers still dominating the detection rates). This model makes the assumption that CE events with HG donors do not always end in a premature merger, allowing more binaries to survive the CE and form merging DCOs, and therefore increasing

TABLE 2
DETECTION RATES FOR SECOND-GENERATION DETECTORS IN THE *high-end* METALLICITY SCENARIO

Model	AdV [$\rho \geq 8$] $f_{\text{cut}} = 20$ Hz		KAGRA [$\rho \geq 8$] $f_{\text{cut}} = 10$ Hz		aLIGO [$\rho \geq 8$] $f_{\text{cut}} = 20$ Hz			3-det network [$\rho \geq 10(12)$] $f_{\text{cut}} = 20$ Hz	
	Insp yr ⁻¹	PhC (EOB) yr ⁻¹	Insp yr ⁻¹	PhC (EOB) yr ⁻¹	Insp yr ⁻¹	PhC (EOB) yr ⁻¹	PhC (spin) yr ⁻¹	Insp yr ⁻¹	PhC yr ⁻¹
NS-NS									
Standard	0.3	0.3	0.8	0.7	1.2	1.1	-	2.5 (1.5)	2.4 (1.4)
Optimistic CE	0.9	0.9	2.1	1.9	3.3	3.1	-	6.9 (4.0)	6.5 (3.8)
Delayed SN	0.4	0.4	1.0	0.9	1.6	1.5	-	3.3 (1.9)	3.1 (1.8)
High BH Kicks	0.3	0.3	0.7	0.7	1.1	1.1	-	2.3 (1.4)	2.2 (1.3)
BH-NS									
Standard	0.2	0.2	0.5	0.4	0.7	0.6	0.8	1.5 (0.9)	1.2 (0.7)
Optimistic CE	1.1	1.0	2.9	2.2	4.4	3.6	4.4	9.2 (5.4)	7.4 (4.3)
Delayed SN	0.09	0.07	0.2	0.2	0.4	0.3	0.5	0.8 (0.5)	0.6 (0.3)
High BH Kicks	0.01	0.007	0.02	0.02	0.04	0.03	0.1	0.09 (0.05)	0.07 (0.04)
BH-BH									
Standard	35	41 (38)	70	93 (86)	117	148 (142)	348	236 (144)	306 (177)
Optimistic CE	126	144 (133)	281	366 (333)	491	618 (585)	1554	1042 (588)	1338 (713)
Delayed SN	27	34 (32)	50	81 (75)	90	129 (124)	320	182 (110)	270 (155)
High Kick	0.6	1.0 (0.9)	0.9	2.5 (2.3)	2.1	3.8 (3.8)	12	4.2 (2.7)	8.2 (4.7)

^a Detection rates computed for the high-end metallicity evolution scenario using the inspiral (“Insp”) and PhC or EOB IMR models for nonspinning binaries. For aLIGO we also list rough upper limits on the rates computed with the IMR PhC model by assuming that BHs have near-maximal aligned spins ($\chi_1 = \chi_2 = 0.998$ for BH-BH systems; $\chi_1 = 0.998$ and $\chi_2 = 0$ for BH-NS systems). The inspiral is calculated using the restricted PN approximation, which overestimates the amplitude (and therefore the detection rates) for low-mass systems (NS-NS) when compared to the full IMR calculations; cf. Section 3 for details. The last two columns were computed assuming a minimum *network* SNR of 10 (or 12, in parentheses) for a three-detector network composed of three instruments located at the LIGO Hanford, LIGO Livingston, and Virgo sites, all with aLIGO sensitivity. For each detector, f_{cut} is the assumed low-frequency cutoff in the power spectral density: see section 5.2.

TABLE 3
DETECTION RATES FOR SECOND-GENERATION DETECTORS IN THE *low-end* METALLICITY SCENARIO

Model	AdV [$\rho \geq 8$] $f_{\text{cut}} = 20$ Hz		KAGRA [$\rho \geq 8$] $f_{\text{cut}} = 10$ Hz		aLIGO [$\rho \geq 8$] $f_{\text{cut}} = 20$ Hz			3-det network [$\rho \geq 10(12)$] $f_{\text{cut}} = 20$ Hz	
	Insp yr ⁻¹	PhC (EOB) yr ⁻¹	Insp yr ⁻¹	PhC (EOB) yr ⁻¹	Insp yr ⁻¹	PhC (EOB) yr ⁻¹	PhC (spin) yr ⁻¹	Insp yr ⁻¹	PhC yr ⁻¹
NS-NS									
Standard	0.3	0.3	0.7	0.6	1.1	1.0	-	2.3 (1.3)	2.2 (1.3)
Optimistic CE	0.8	0.7	1.8	1.7	2.9	2.7	-	6.0 (3.5)	5.6 (3.3)
Delayed SN	0.4	0.4	1.0	0.9	1.5	1.4	-	3.2 (1.8)	2.9 (1.7)
High BH Kicks	0.3	0.3	0.7	0.6	1.0	1.0	-	2.1 (1.3)	2.0 (1.2)
BH-NS									
Standard	0.3	0.2	0.7	0.5	1.1	0.8	1.2	2.3 (1.3)	1.8 (1.0)
Optimistic CE	1.4	1.2	3.6	2.8	5.5	4.4	5.7	12 (6.7)	9.4 (5.4)
Delayed SN	0.2	0.1	0.5	0.4	0.8	0.6	0.9	1.7 (0.9)	1.3 (0.7)
High BH Kicks	0.04	0.03	0.09	0.07	0.1	0.1	0.3	0.6 (0.2)	0.5 (0.2)
BH-BH									
Standard	56	66 (61)	106	153 (140)	183	246 (235)	610	369 (226)	514 (292)
Optimistic CE	287	324 (297)	629	828 (745)	1124	1421 (1339)	3560	2384 (1336)	3087 (1633)
Delayed SN	53	64 (59)	97	152 (139)	171	241 (231)	596	345 (213)	501 (291)
High Kick	0.9	1.5 (1.4)	1.4	3.8 (3.6)	3.2	5.9 (5.8)	19	6.6 (4.0)	13 (7.2)

^a Same as Table 2, but for the *low-end* metallicity scenario.

detection rates. As a result the Optimistic CE model yields very large BH-BH rates, comparable to, though a factor of a few below, existing upper limits on the BH-BH binary mergers from initial LIGO/Virgo observations (see, e.g., Belczynski et al. 2012a; Abadie et al. 2012; Aasi et al. 2013a).

Our quantitative predictions for compact binary merger rates are consistent with our previous papers in this series (Dominik et al. 2012, 2013). In particular, we agree with the main conclusion of those papers: detectable BH-BH binaries can be formed over a broad range of metallicities, with a significant proportion forming in highly subsolar environments (Fig. 7). On a model-by-model basis our results are in good agreement with prior work, with factor-of-two or smaller differences due to our inclusion of cosmological effects.

As expected, the simple approximation of Eq. (3) gives

a good order-of-magnitude estimate of the NS-NS detection rates listed in Tables 2 and 3. However, the approximation fails for BH-BH systems. By comparing the detection rates from Table 1 with inspiral rates from Tables 2 and 3, we see that the local Universe approximation of Eq. (3) overestimates more careful calculations of detection rates by a factor ~ 2 for BH-BH systems. The limited signal bandwidth of high-mass systems, the redshift dependence of binary merger rates, and cosmological corrections make simple scaling relations inaccurate over the large volume in which detectors are sensitive to BH-BH systems. On the other hand, as the merger-ringdown phase of these binaries falls within the sensitive band of second-generation interferometers, it provides a significant contribution to the SNR. Indeed, as can be seen in Tables 2 and 3, the full IMR calculations increase the detection rates considerably. However, BH-BH detec-

tion rates computed with appropriate cosmological corrections are still lower than local merger rates converted into detection rates via the basic scaling of Eq. (3).

5.2. Impact of waveform models on predicted rates

Our results show that the merger-ringdown contribution is not important for estimating detection rates of DCOs containing NSs. In fact, when compared with the restricted PN model, the IMR waveforms slightly *decrease* event rates for NS-NS and BH-NS systems. The reason for this reduction is that IMR waveforms (such as PhC and EOB) provide a more accurate representation of the early inspiral, incorporating PN amplitude corrections that *reduce* the signal amplitude¹—and hence the event rates—for signals dominated by the early inspiral.

BH-NS systems may be subject to an additional event rate reduction mechanism. There is the possibility of the NS being distorted and disrupted by the BH tidal field. When these violent phenomena occur, a suppression of the GW amplitude takes place before the ISCO frequency, and the SNR decreases with respect to that of a BH-BH system with the same properties. The GW shut-off due to NS tidal disruption depends on the parameters of the system: large values of the mass ratio, the BH spin, and the NS radius all favor NS disruption. By using point-particle IMR waveforms to describe the GW emission of BH-NS systems we are neglecting this event rate reduction mechanism. While it would be possible to take these effects into account for nonspinning systems by using the GW amplitude model of Pannarale et al. (2013), accurate models for systems with spinning BHs do not exist yet. For consistency we therefore use BH-BH waveform models in both cases. Additionally, Pannarale et al. (2013) found that in the nonspinning case, the SNR difference between the mergers of disrupted BH-NS systems and the undisrupted systems modeled with PhC is less than 1%.

Including the merger portion of the signal is important for BH-BH systems. For illustration, let us focus on the Standard Model: if we use PhC waveforms rather than the restricted PN approximation, we find a $\sim 25\%$ increase in the detection rates of BH-BH systems, from 117 (183) to 148 (246) in the *high-end* (*low-end*) metallicity scenario.

The rates predicted by EOB and PhC models agree quite well². This can be understood by looking again at Figure 2, which shows that different approximations of the strong-field merger waveform agree rather well (at least in the equal-mass limit) on the SNR ρ and hence on the predicted event rates, which scale with the cube of the SNR. Waveform differences produce systematic rate uncertainties significantly less than a factor of 2, much smaller than astrophysical differences between our preferred models.

Our detailed calculation shows that typically PhC model overestimate the rates by about 10% when com-

¹ Note that in Eq. (3.14) of Santamaría et al. (2010) the coefficient of the dominant correction, \mathcal{A}_2 , listed in their Eq. (A5) is negative.

² We also carried out calculations using PhB models, which overestimate rates by about 10% with respect to PhC models. We decided not to report these results in the Tables, because the PhB model is less accurate than PhC, although it is easier to implement and less computationally expensive.

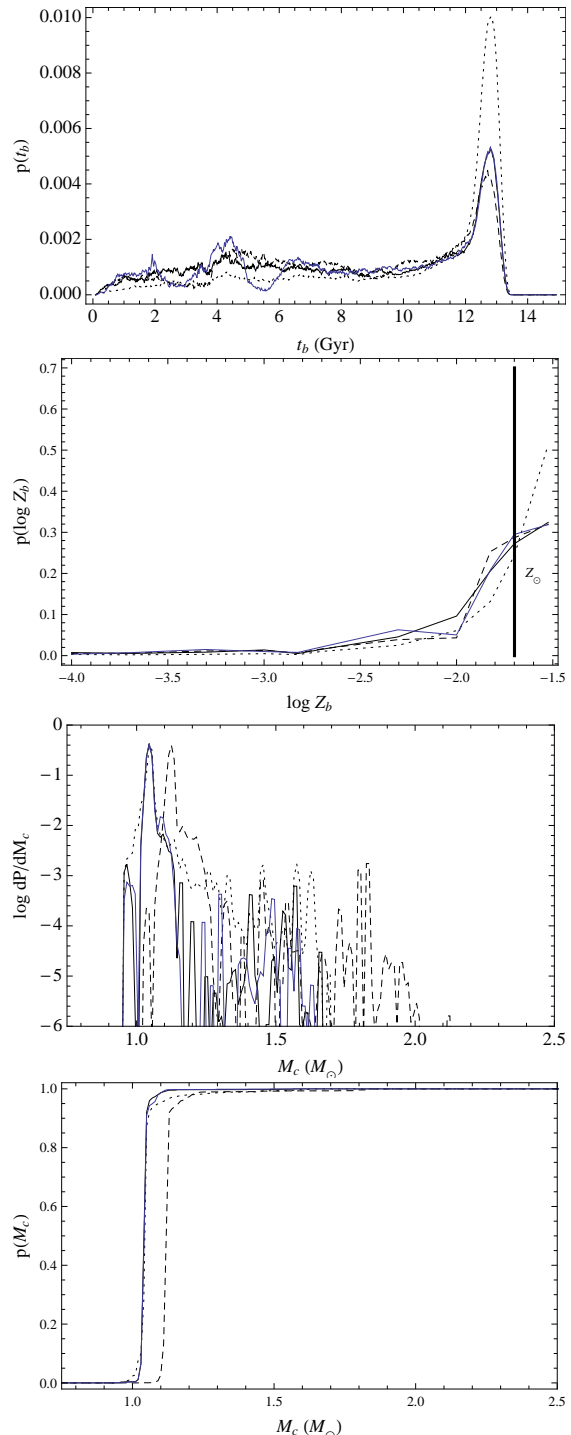


FIG. 5.— **Compact NS-NS binaries detectable by aLIGO:** Properties of NS-NS binaries with $\rho \geq 8$ in a single aLIGO instrument in the high-end metallicity scenario, scaled in proportion to their detection probability. Different color and line styles indicate results for different binary evolution models: Standard model (solid black), Optimistic CE scenario (dotted black), delayed SN (dashed black), and high BH kicks (blue). The top, second, and third panels show the distribution of birth time t_b , birth metallicity Z_b (with a vertical bar marking solar metallicity, $Z_\odot = 0.02$), and chirp mass M_c , respectively. The bottom panel shows the cumulative distribution in chirp mass, to highlight significant changes on a linear scale. The time domain ranges from 0 Gyr (Big Bang) to 13.47 Gyr (today). Though our simulations use a discrete array of metallicity bins, to guide the eye their relative contributions have been joined by solid lines in the second panel; this histogram makes no correction for the density of metallicity bins.

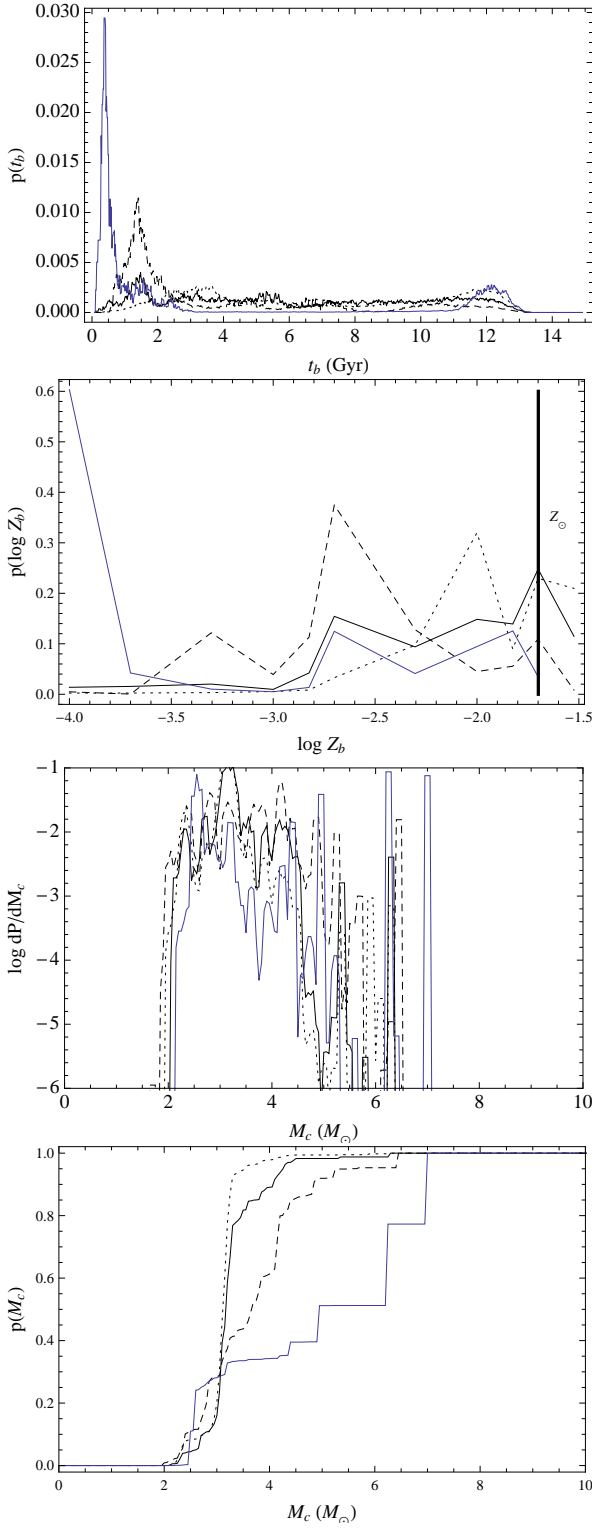


FIG. 6.— Compact BH-NS binaries detectable by aLIGO: Same as Figure 5, but for BH-NS binaries in the high-end metallicity scenario. Some of the sharp features in the chirp mass distribution are an artifact of the crude binning in metallicity undertaken for computational reasons; see the discussion in section 5.3.

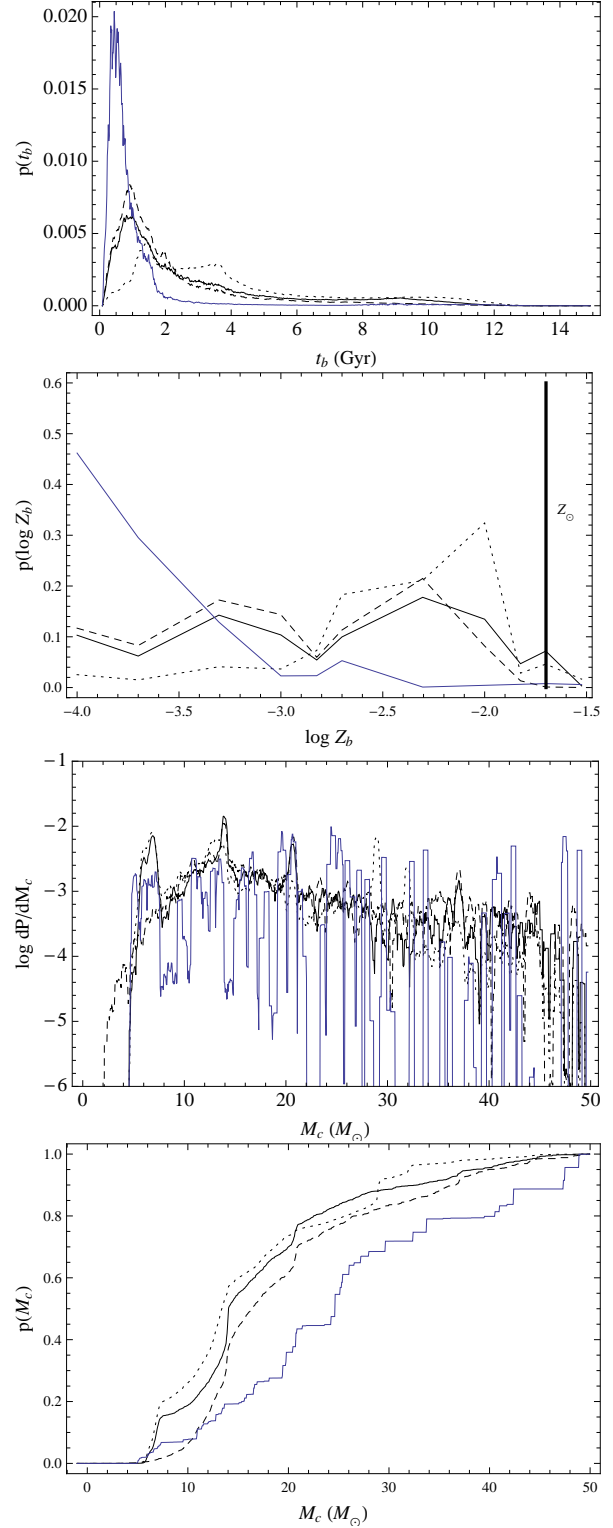


FIG. 7.— BH-BH binaries detectable by aLIGO: Same as Figure 5, but for BH-BH binaries in the high-end metallicity scenario. Some of the sharp features in the chirp mass distribution are an artifact of the crude binning in metallicity undertaken for computational reasons; see the discussion in section 5.3.

pared to EOB models. This agreement is nontrivial, because the two families of models are very different in spirit and construction: the PhC family is a frequency-domain model that can be easily implemented in rate calculations, while the time-domain EOB model is more accurate in its domain of validity and more computationally demanding. It is important to note that in order to use the two families of models in rate calculations we must compute waveforms and SNRs in regions of the parameter space where the models were not tuned to numerical relativity simulations. In particular, both models become less accurate for small mass-ratio binaries.

Besides systematic errors in waveform modeling, the detection rates reported in this work (and the resulting distribution of detectable DCO parameters) depend on our detection criteria. We ignore a variety of complications of the detection pipelines, such as the difficulty of searching for precessing sources, noise artifacts (non-stationary, non-Gaussian “glitches” in the instruments) which can make searches for shorter, high-mass signals less sensitive, and the limited uptime of detectors. Instead, we have assumed several simplistic detection thresholds on single-detector or network SNR that are constant across all masses and mass ratios.

Moreover, achieving good detector sensitivity at low frequencies may prove particularly difficult. We have only included bandwidth above specified low-frequency cutoffs ($f_{\text{cut}} = 20$ Hz in most cases) for detection-rate calculations. However, the specific choice of low frequency cutoff has minimal impact on our results. For example, using a lower cutoff $f_{\text{cut}} = 10$ Hz rather than $f_{\text{cut}} = 20$ Hz in the single-detector, high-end metallicity aLIGO rate calculation would increase the Standard Model BH-BH rates from 117 to 128 in the inspiral case, and from 148 to 161 in the IMR case. The effect is even smaller for BH-NS and NS-NS rates.

The impact of spins on the predicted detection rates can be important. We only consider BH spins, since NSs in compact binaries are not expected to be rapidly spinning (e.g., Mandel & O’Shaughnessy 2010) and the dynamical impact of NS spin will be small. In Tables 2 and 3 we use the PhC model to estimate the possible impact of BH spin on BH-NS and BH-BH detection rates by assuming that all BHs are nearly maximally spinning (i.e., with dimensionless spin parameter $\chi_1 = \chi_2 = 0.998$) and aligned with the orbital angular momentum. Aligned BH spins cause an orbital hang-up effect that increases the overall power radiated in the merger, produces a rapidly spinning merger remnant, and therefore increases the range to which high-mass binaries can be detected.

We find that spin effects may increase BH-BH detection rates by as much as a factor of 3. These increased rates are a direct result of the increased horizon distance to spinning binaries. For example, a $(30+30) M_{\odot}$ binary can be observed to roughly 1.3 times farther and be detected $\simeq (1.3)^3 \simeq 2$ more often with near-maximal spins than with zero spin. Additionally, spin dynamics can provide a direct diagnostic of the dominant physical effects in DCO formation (Gerosa et al. 2013). Spin effects only marginally increase BH-NS rates, but (as discussed at the beginning of this section) tidal disruption, which we neglected, may have the opposite effect.

5.3. Astrophysical properties of observable DCOs

We now turn to a more detailed analysis of the observable properties of DCOs. For concreteness we will focus on aLIGO results for the “Standard model” and nonspinning PhC waveforms, unless stated otherwise.

NS-NS. By comparing Tables 2 and 3 we see that the detection rates of NS-NS systems are not sensitive to our differing metallicity evolution scenarios. For simplicity, we therefore only discuss our results for the *high-end* metallicity evolution scenario.

As shown in our previous work (Dominik et al. 2012), NS-NS systems are efficiently created in metal-rich environments. The observable population shares this trait, and half of the observable systems originate from solar metallicities and higher. As the average metallicity content of the Universe correlates with time and as most DCOs preferentially merge shortly after formation (i.e., the time delay distribution is $\propto t_{\text{merger}}^{-1}$; see Dominik et al. (2012)), the birth rate of detectable NS-NS systems peaks at 13 Gyrs after the Big Bang (see Fig. 5). The most distant detectable system has a merger redshift $z \sim 0.13$.

The range of possible chirp masses in the third panel from the top of Figure 5 is limited at the low end ($> 0.87 M_{\odot}$) by our assumed $1 M_{\odot}$ minimum birth mass for NSs, and is limited at the high end by the maximum mass for a NS ($m_{\text{NS}} < 2.5 M_{\odot}$; $\mathcal{M}_c < 2.1 M_{\odot}$). The birth mass, in turn, is set by supernova physics, which we have implemented as the Rapid or Delayed SN engine (Fryer et al. 2012a). For this reason the NS mass difference between the SN engines is intrinsic to the entire merging population of NS-NS systems. Therefore, this observable feature should be available to any of the detectors considered in this study.

The chirp mass distributions for Standard and Optimistic CE models span the range from $0.9 M_{\odot}$ to $1.6 M_{\odot}$. The Delayed SN model results in a notably different NS mass distribution, favoring heavier masses. As the SN explosion in the Delayed engine lasts longer, more matter is accreted onto the proto-NS (which is more massive than in the Rapid engine scenario), allowing the formation of more massive remnants (cf. Figure 5). The maximum allowed NS mass in this model is $2.5 M_{\odot}$, and in extreme (but very rare) cases this mass is approached; the maximum chirp mass for a detectable system in our Monte Carlo simulation was $2.1 M_{\odot}$, corresponding to both components close to the maximum allowed limit. For comparison, chirp masses of NS-NS systems in the models utilizing the Rapid SN engine (Standard, Optimistic CE and High BH kick) never exceed $1.7 M_{\odot}$. Such extremely high masses are rare for all engines, however, and the majority of chirp masses are much lower, as seen in Figure 5. The presence of more massive systems in the Delayed SN models extends the horizon of NS-NS detectability to $z \sim 0.16$.

Lastly, we note that Standard and High BH kick models are identical for NS-NS systems. The difference between the black curve (Standard) and blue curve (High BH Kick) in Figure 5 corresponds to the systematic errors associated with Monte Carlo errors of binary simulations, galaxy sampling, metallicity binning, etc.

BH-NS. In our previous study (Dominik et al. 2013) we showed that BH-NS systems are efficiently created

at moderate metallicities ($Z \sim 0.1 Z_{\odot}$, or $\log(Z) \sim -2.7$). Indeed, Figure 6 shows that about half of all detectable BH-NS systems will originate from metallicities $Z < 0.5 Z_{\odot}$ ($\log(Z) < -2$). These systems have higher chirp masses than NS-NS systems, on average $3.3 M_{\odot}$ vs. $1.2 M_{\odot}$, and therefore the detectors can sample BH-NS systems from a larger volume. However, BH-NS systems are the rarest of all DCOs per unit (comoving) volume. As a consequence, BH-NS binaries typically yield the lowest detection rates. One exception is the Optimistic CE model, in which the merger rate per unit volume is large enough (while still being lower than for NS-NS systems at all redshifts) that BH-NS detection rates are larger than NS-NS rates because they are observed farther (cf. Table 1 and Figure 6).

In our standard model BH-NS systems are detectable up to redshift $z \approx 0.28$. However, in the Delayed SN model this value reaches $z \approx 0.31$. As discussed earlier, this is due to the more massive NSs (up to $2.4 M_{\odot}$) produced by the Delayed engine.

BH-BH. As discussed in our previous papers in this series (Belczynski et al. 2010; Dominik et al. 2012, 2013), BH-BH systems are formed most efficiently in low-metallicity environments. The detectable population reflects this property: about half of all detectable BH-BH systems were created in environments with metallicities $Z < 0.1 Z_{\odot}$ ($\log(Z) < -2.7$). As in prior studies (Belczynski et al. 2010; Dominik et al. 2012, 2013; Voss & Tauris 2003b), our calculations imply that BH-BH systems yield the highest detection rates for ground-based interferometers. This is true even in the “High BH kick” model, where the vast majority of binaries containing a BH are disrupted.

Adjusting the metallicity evolution in the Universe from *high-end* to *low-end* we see a factor of ~ 2 increase in detection rates. In the *low-end* scenario the average metallicity in the Universe is lower at all times. Low metallicity environments are much more effective at producing merging BH-BH systems than higher ones, hence the increase in the detection rates.

Half of the detectable objects have chirp masses above $14 M_{\odot}$. The most massive of these systems originate from environments with very low metallicity content ($Z \sim 0.01 Z_{\odot}$). The birth times of detectable BH-BH systems peak at ~ 1 Gyr after the Big Bang. Additionally, half of these systems were created within ~ 2 Gyrs of the Big Bang (see top panel of Figure 7), when the average abundance of heavy elements was much smaller than today.

As seen in Tables 2 and 3, the detection rates of BH-BH systems vary as we change our assumptions between the four models and two metallicity evolution scenarios. We can distinguish two extreme configurations: (1) The High BH kick model yields the lowest rates of merging BH-BH systems. This is a direct consequence of assuming the presence of the maximum natal kick velocities allowed within our framework, which efficiently disrupt BH progenitor binaries. (2) The highest detection rate is achieved with the Optimistic CE model. Here it is assumed that binaries are allowed to progress through the CE with a HG donor, which adds a significant amount of BH-BH systems to the detectable population. The detection rates of the other two models (Standard and

Delayed SN) are similar to each other.

The farthest objects are detectable out to $z \sim 2$. These systems consist of the most massive BH pairs ($m_1 = 61 M_{\odot}$ and $m_2 = 66 M_{\odot}$ in the detectable population, with a chirp mass equal to $55 M_{\odot}$), born 1.8 Gyr after the Big Bang, and originating from regions with the lowest metallicity content ($Z = 0.005 Z_{\odot}$). Note that the maximum mass of BH-BH systems is limited by the maximum ZAMS mass of stars, which was set to $150 M_{\odot}$ in the StarTrack code (cf. Belczynski et al. 2014).

The detectable BH-BH chirp mass distribution for the Standard model has three major peaks. These are present at $\sim 7 M_{\odot}$, $14 M_{\odot}$, and $21 M_{\odot}$ (see the black curve in the 3rd and 4th panels of Fig. 7). Their presence is associated with the physics governing the Rapid SN engine and the formation of the most massive BH-BH systems. Within this framework we can distinguish three scenarios for BH formation, each depending on the pre-SN carbon-oxygen (CO) mass (see Eq. 16 in Fryer et al. (2012a)). The “A” scenario occurs for $6 M_{\odot} < M_{\text{CO}} \leq 7 M_{\odot}$ and results in full fallback on the BH and, therefore, no natal kicks (see Eq. 1). The “B” scenario occurs for $7 M_{\odot} < M_{\text{CO}} \leq 11 M_{\odot}$, where the fallback is partial and some natal kicks are present. For this scenario we expect a decreased number of BH-BH systems because of natal kicks disrupting binary systems during SNe. The “C” scenario develops for $M_{\text{CO}} \geq 11 M_{\odot}$ and again results in full fallback, and no natal kicks.

BH progenitors originating from Z_{\odot} environments never form through the C scenario, since they lose mass in winds at rates that do not allow them to form CO cores larger than $11 M_{\odot}$. Since BH-BH progenitors in the B scenario are subject to disruption due to the presence of natal kicks, most BH-BH systems in Z_{\odot} environments form through the A scenario, with chirp masses clustered around $7 M_{\odot}$.

However, reducing the metallicity by a factor of 2 lowers the wind mass loss rates sufficiently to allow BHs to form through the C scenario. At this metallicity ($\sim 0.5 Z_{\odot}$) only the most massive progenitors ($M_{\text{ZAMS}} > 100 M_{\odot}$) may form BHs through this scenario. Additionally, the mass of the BHs formed from these high mass components ($M_{\text{ZAMS}} > 100 M_{\odot}$) only depends weakly on their initial mass. This stems from the fact that these stars evolve quickly (\sim Myrs) and lose large fractions of their hydrogen envelope. Binary evolution does not alter this result significantly, as the interactions between components, such as mass transfer during CE episodes, also lead to the removal of their hydrogen envelopes. The result for metallicity $\sim 0.5 Z_{\odot}$ is a clustering of BH-BH systems formed from the most massive binaries at masses around $16 M_{\odot}$ for each component. This produces the peak in the chirp mass distribution at $\sim 14 M_{\odot}$.

Reducing the metallicity content by another factor of 2 (to $\sim 0.25 Z_{\odot}$) allows the same mechanism to form BH-BH systems with masses clustering at around $24 M_{\odot}$ for each component. These systems form the peak in the chirp mass distribution at $\sim 21 M_{\odot}$.

The grouping effect disappears when reducing the metallicity abundance in BH progenitors even further. For example, at $0.1 Z_{\odot}$ the low wind mass loss rate does not increase the separation between components as significantly as for higher metallicities. Consequently, the

most massive progenitor binaries engage in a CE phase early in their evolution. This usually happens when the donor is on the HG and the Standard model does not allow for successful outcomes of such CEs. However, this scenario is allowed to form BH-BH systems in the Optimistic CE model, yielding the peak present in the chirp mass distribution at $\sim 29 M_{\odot}$.

As discussed above, the chirp mass distribution in scenario *C* depends sensitively on the mass loss rate of stars, which depends strongly on metallicity. Binary evolution for $0.5 Z_{\odot}$ and $0.25 Z_{\odot}$ creates sharp peaks in the chirp mass distribution of BH-BH systems. In the discrete metallicity grid simulated in this study, there are no metallicity points between $0.5 Z_{\odot}$ and $0.25 Z_{\odot}$. Targeted follow-up investigations indicate that metallicity choices between $0.5 Z_{\odot}$ and $0.25 Z_{\odot}$ lead to additional sharp peaks in the chirp mass distribution between $14 M_{\odot} - 21 M_{\odot}$. We expect that an integral over a fine grid with appropriately small step sizes in metallicity would lead to all of these narrow peaks merging together to form a single broad distribution without sharp features. However, we cannot confidently describe the shape of this distribution without a more detailed investigation with a fine grid of metallicities, which is not computationally tractable at present.

Finally, the peak in the chirp mass distribution at $\sim 7 M_{\odot}$ in the Standard model is formed from systems born in $0.5-1 Z_{\odot}$ environments. These are low-mass BHs (usually $8-9 M_{\odot}$ per component) formed in the *A* scenario. This formation is particularly interesting as it does not appear in the Delayed SN model, with the difference stemming from the different fallback scenarios in the Rapid and Delayed engines. With the Rapid engine, we can distinguish the three fallback regions. However, the Delayed engine predicts one region of partial fallback for $3.5 M_{\odot} < M_{\text{CO}} \leq 11 M_{\odot}$ and one region of full fallback $M_{\text{CO}} \geq 11 M_{\odot}$ (identical to the *C* scenario in the Rapid engine). Since partial fallback implies the presence of natal kicks and, therefore, increased probability of binary disruption, there are no “preferred” masses for the lightest BHs in the Delayed SN engine (see dashed line on the 3rd panel, Fig. 7) as in the Rapid engine.

The Standard and Delayed SN models also yield different lower mass limits for BH remnants (see Section 2). For the “Rapid engine” scenario the lowest-mass BH is $\sim 5 M_{\odot}$, while for the “Delayed engine” scenario the lowest-mass BH is $\sim 2.5 M_{\odot}$ (this is also the highest NS mass adopted in our *StarTrack* calculations). As a result, the detectable systems with the lowest total mass have $\mathcal{M}_c = 4.8 M_{\odot}$ and $\mathcal{M}_c = 2.4 M_{\odot}$ in the Rapid and Delayed engine scenarios, respectively.

6. CONCLUSIONS

We have calculated cosmological detection rates of merging DCOs for second-generation GW observatories. We used redshift distributions of merging DCOs from the *StarTrack* population synthesis code, and have incorporated the cosmic star formation rate as well as galaxy and metallicity evolution. Using state-of-the-art gravitational waveforms and detector sensitivity curves, we have translated the cosmological merger rates into detection rates for four distinct models of binary evolution.

Our study has several robust implications for imminent GW searches. First and foremost, our four models agree

on the detection rates of merging NS-NS systems, with the exception of the Optimistic CE model which predicts rates a factor of 2–3 times higher than other models. The mass distributions of detectable NS-NS systems are also similar across models, with the exception of the Delayed SN model, which allows for the formation of NSs with higher masses due to prolonged accretion during the SN explosion. We predict that NS-NS binaries will be detectable up to redshift $z \approx 0.13$, i.e., only in the local Universe.

Second, BH-NS systems are expected to be the rarest detectable DCOs, with the exception of the Optimistic CE model, in which BH-NS detection rates slightly exceed those of NS-NS systems. We predict BH-NS systems to be detectable up to redshift $z \approx 0.3$.

In contrast, BH-BH systems will provide the largest number of detections, making them the primary target for first detection and the most promising source for future statistical studies of source populations. BH-BH binaries dominate event rates even in the pessimistic “High BH kick” model, wherein most of the systems containing BHs are disrupted during the SN. Additionally, the BH-BH mass distribution could have rich, observationally-accessible structure (various lower limits and shapes) that encodes fine details about stellar and binary evolution (see, e.g., O’Shaughnessy 2012; Belczynski et al. 2012d; Kreidberg et al. 2012; Fryer et al. 2012b). We note, however, that the crude binning in metallicity that we had to undertake in order to limit computational costs may create artificial sharp, narrow features in the mass distribution, which would merge together into broader trends with a finer metallicity grid.

Our study shows that detectable NS-NS systems are formed significantly later in the history of the Universe than BH-BH and BH-NS systems. As shown in Figs. 5, 6, and 7, the birth times of NS-NS systems cluster around 13 Gyr after the Big Bang, while for the other systems this is 1 Gyr. This behavior might be counterintuitive, as the intrinsic distribution of time delays between formation and merger for DCOs falls off as t_{merger}^{-1} , barring exceptional circumstances (e.g., near-solar metallicity BH-BH binaries, Dominik et al. 2012). Therefore, one might expect the majority of detectable DCOs to be formed within the past \sim Gyr as is the case for NS-NS systems. However, BH-BH systems are created most efficiently in the lowest metallicity environments, and therefore their formation rate is highest in the early Universe. The long time-delay tail of these early systems dominates the subsequent detection rate. The metallicity evolution is therefore a crucial factor in predicting the detectable rate of DCOs.

We also find that including the merger and ringdown components of the GW signal does not have a significant impact on the detection rates of NS-NS systems. The full IMR calculations become important for higher mass systems, and especially for BH-BH binaries. The detection rates for BH-BH systems increases by at least 20%, and typically by $\sim 50\%$, when using full IMR waveforms when compared to the PN inspiral alone.

The detection rate of BH-BH systems is also sensitive to spin effects. Extreme aligned spins increase the rates by a factor of ~ 3 when compared with the non-spinning case.

We used simplified criteria for detectability, considering an SNR threshold of 8 in a single detector as a proxy for the network (cf. Abadie et al. 2010). For reference, we also considered a network SNR threshold of 10, which is likely to be very optimistic, and 12, which is more realistic (cf. Aasi et al. 2013b), on a network of three detectors with aLIGO sensitivity. The network SNR threshold of 12 yields rates which are roughly comparable with rates computed using an SNR threshold of 8 in a single aLIGO detector as proxy for the network. The actual detection thresholds are a complicated function of network configuration, the level and frequency of non-Gaussian, non-stationary excursions in the noise, and search pipeline sensitivity to different source types. Therefore, our simple thresholds are only meant to yield rough estimates of detection rates, and the focus should be on relative rates for different source types and model assumptions rather than absolute numbers. Finally, we note that the sensitivity of advanced detectors will gradually improve during commissioning, and several years will pass before they reach the sensitivity we have assumed above (for an approximate time line, see Aasi et al. 2013b).

The detection rates computed by assuming an SNR threshold of 8 in a single aLIGO detector as proxy for the network allow for a direct comparison with the rate ranges compiled in (Abadie et al. 2010), which used the same detectability criterion. Abadie et al. (2010) incorporated a number of population synthesis studies and Galactic binary pulsar observations, but did not include some of the factors considered in the present study, such as cosmology and variations in metallicity distributions and star formation rates with redshift. We find that our predicted detection rates for NS-NS and BH-BH binaries fall within the ranges given in (Abadie et al. 2010) for all models and both metallicity distribution choices considered in the present work. For BH-NS binaries, the same holds for all models and metallicity choices except for the high BH kick model, which yields BH-NS detection rates below the range quoted in (Abadie et al. 2010).

We note that uncertainties in waveform systematics and detection criteria pale in comparison to uncertainties in stellar and binary evolution. We consider the most important uncertainties to be the progress and outcome of the CE phase, the SN explosion mechanism and the magnitude of BH natal kicks. The four binary evolution models discussed in this study explore these uncertainties, resulting in a wide range of mass distributions and event rates. Changing other parameters such as the initial binary mass distribution or varying the mass escaping the systems during mass transfer episodes

would also influence the resulting distributions and rates (O’Shaughnessy et al. 2005, 2008, 2010b).

The properties of the DCO populations produced in our various models are sufficiently differentiated that it may be possible to constrain or rule out some of the input physics based on observed populations. For example, a lack of detections will disfavor the Optimistic CE model, in which we allow for CE events with HG donors and thus find very high detection rates. This would suggest that such donors need to have a well defined core-envelope structure in order to avoid a merger during this phase. If BH-BH systems are not detected far more frequently than other DCO types, a likely explanation is that BHs receive significant natal kicks disrupting their binaries. A detailed comparison of detection rates with current LIGO upper limits can be found in Belczynski et al. (2012b). As detections accumulate, a well measured chirp mass distribution could allow us to distinguish between the Rapid and Delayed SN engine models, which generate continuous and gapped chirp mass distribution of DCOs, respectively. The number of detections needed to distinguish between the Rapid and Delayed SN engines will be discussed in future work (Dominik et al. 2014, in preparation).

We thank a number of LIGO and Virgo collaboration colleagues, particularly Thomas Dent, David Shoemaker, Stephen Fairhurst and Peter Saulson, for advice on the manuscript. We thank the N. Copernicus Astronomical Centre in Warsaw, Poland, and the University of Texas at Brownsville, for providing computational resources. The authors acknowledge the Texas Advanced Computing Center (TACC) at The University of Texas at Austin for providing computational resources. KB and MD acknowledge support from MSHE grant N203 404939 and N203 511238, NASA Grant NNX09AV06A to the UTB, Polish Science Foundation Master 2013 Subsidy and National Science Center DEC-2011/01/N/ST9/00383. EB acknowledges support from National Science Foundation CAREER Grant PHY-1055103. ROS was supported by NSF award PHY-0970074 and the UWM Research Growth Initiative. DEH acknowledges support from National Science Foundation CAREER grant PHY-1151836. He was also supported in part by the Kavli Institute for Cosmological Physics at the University of Chicago through NSF grant PHY-1125897 and an endowment from the Kavli Foundation and its founder Fred Kavli. TB was supported by the DPN/N176/VIRGO/2009 grant. FP was supported by STFC Grant No. ST/L000342/1.

REFERENCES

- Aasi, J., Abadie, J., Abbott, B. P., et al. 2013a, *Phys. Rev. D*, 87, 022002
—, 2013b, (arXiv:1304.0670)
Abadie, J., Abbott, B. P., Abbott, R., et al. 2012, *Phys. Rev. D*, 85, 082002
—, 2010, *Classical and Quantum Gravity*, 27, 173001
Ajith, P. 2011, *Phys. Rev. D*, 84, 084037
Ajith, P. & Bose, S. 2009, *Phys. Rev. D*, 79, 084032
Ajith, P., Hannam, M., Husa, S., et al. 2011, *Physical Review Letters*, 106, 241101
Amaro-Seoane, P. & Freitag, M. 2006, *ApJ*, 653, L53
Bailyn, C. D., Jain, R. K., Coppi, P., & Orosz, J. A. 1998, *ApJ*, 499, 367
Belczynski, K., Buonanno, A., Cantiello, M., et al. 2014, *ArXiv e-prints*
Belczynski, K., Dominik, M., Bulik, T., et al. 2010, *ApJ*, 715, L138
Belczynski, K., Dominik, M., Repetto, S., Holz, D. E., & Fryer, C. L. 2012a, *ArXiv e-prints*
—, 2012b, *ArXiv e-prints*
Belczynski, K., Kalogera, V., Rasio, F. A., et al. 2008, *ApJS*, 174, 223

- Belczynski, K., Taam, R. E., Kalogera, V., Rasio, F. A., & Bulik, T. 2007, *ApJ*, 662, 504
- Belczynski, K., Wiktorowicz, G., Fryer, C. L., Holz, D. E., & Kalogera, V. 2012c, *ApJ*, 757, 91
- . 2012d, *ApJ*, 757, 91
- BICEP2 Collaboration, Ade, P. A. R., Aikin, R. W., et al. 2014, *ArXiv e-prints*
- Capano, C., Pan, Y., & Buonanno, A. 2013
- Cutler, C. & Flanagan, É. E. 1994, *Phys. Rev. D*, 49, 2658
- Damour, T., Nagar, A., & Trias, M. 2011, *Phys. Rev.*, D83, 024006
- De Donder, E. & Vanbeveren, D. 2004, *New Astronomy Review*, 48, 861
- Dewi, J. D. M. & Pols, O. R. 2003, *MNRAS*, 344, 629
- Dominik, M., Belczynski, K., Fryer, C., et al. 2012, *ApJ*, 759, 52
- . 2013, *ArXiv e-prints*
- Downing, J. M. B., Benacquista, M. J., Giersz, M., & Spurzem, R. 2010, *MNRAS*, 407, 1946
- Finn, L. S. 1996, *Phys. Rev. D*, 53, 2878
- Finn, L. S. & Chernoff, D. F. 1993, *Phys. Rev. D*, 47, 2198
- Flanagan, É. É. & Hughes, S. A. 1998, *Phys. Rev. D*, 57, 4535
- Fontana, A., Salimbeni, S., Grazian, A., et al. 2006, *A&A*, 459, 745
- Fregeau, J. M., Larson, S. L., Miller, M. C., O’Shaughnessy, R., & Rasio, F. A. 2006, *Astrophysical Journal Letters*, 646, L135
- Fryer, C. L., Belczynski, K., Wiktorowicz, G., et al. 2012a, *ApJ*, 749, 91
- . 2012b, *ApJ*, 749, 91
- Gerosa, D., Kesden, M., Berti, E., O’Shaughnessy, R., & Sperhake, U. 2013, *Phys. Rev. D*, 87, 104028
- Grindlay, J., Portegies Zwart, S., & McMillan, S. 2006, *Nature Physics*, 2, 116
- Grishchuk, L. P., Lipunov, V. M., Postnov, K. A., Prokhorov, M. E., & Sathyaprakash, B. S. 2001, *Physics Uspekhi*, 44, 1
- Gültekin, K., Miller, M. C., & Hamilton, D. P. 2004, *ApJ*, 616, 221
- Harry, G. M., for the LIGO Scientific Collaboration. 2010, *Classical and Quantum Gravity*, 27, 084006
- Hobbs, G., Lorimer, D. R., Lyne, A. G., & Kramer, M. 2005, *MNRAS*, 360, 974
- Hogg, D. W. 1999, *ArXiv Astrophysics e-prints*
- Ivanova, N., Heinke, C. O., Rasio, F. A., Belczynski, K., & Fregeau, J. M. 2008, *MNRAS*, 386, 553
- Ivanova, N. & Taam, R. E. 2004, *ApJ*, 601, 1058
- Kreidberg, L., Bailyn, C. D., Farr, W. M., & Kalogera, V. 2012, *ApJ*, 757, 36
- Lyne, A. G., Burgay, M., Kramer, M., et al. 2004, *Science*, 303, 1153
- Mandel, I. & O’Shaughnessy, R. 2010, *Classical and Quantum Gravity*, 27, 114007
- Miller, M. C. & Lauburg, V. M. 2009, *ApJ*, 692, 917
- Nelemans, G., Yungelson, L. R., & Portegies Zwart, S. F. 2001, *A&A*, 375, 890
- Nutzman, P., Kalogera, V., Finn, L. S., Hendrickson, C., & Belczynski, K. 2004, *ApJ*, 612, 364
- O’Leary, R. M., Rasio, F. A., Fregeau, J. M., Ivanova, N., & O’Shaughnessy, R. 2006, *ApJ*, 637, 937
- O’Shaughnessy, R. 2012, Submitted to PRD (arxiv:1204.3117)
- O’Shaughnessy, R., Belczynski, K., & Kalogera, V. 2008, *ApJ*, 675, 566
- O’Shaughnessy, R., Kalogera, V., & Belczynski, K. 2005, *ApJ*, 620, 385
- . 2010a, *ApJ*, 716, 615
- . 2010b, *ApJ*, 716, 615
- O’Shaughnessy, R., Vaishnav, B., Healy, J., & Shoemaker, D. 2010c, *Phys. Rev. D*, 82, 104006
- Özel, F., Psaltis, D., Narayan, R., & McClintock, J. E. 2010, *ApJ*, 725, 1918
- Pan, Y., Buonanno, A., Boyle, M., et al. 2011, *Phys. Rev. D*, 84, 124052
- Pan, Y., Buonanno, A., Buchman, L. T., et al. 2010, *Phys. Rev. D*, 81, 084041
- Pannarale, F., Berti, E., Kyutoku, K., & Shibata, M. 2013, *Phys. Rev. D*, 88, 084011
- Panther, B., Jimenez, R., Heavens, A. F., & Charlot, S. 2008, *MNRAS*, 391, 1117
- Pfahl, E., Podsiadlowski, P., & Rappaport, S. 2005, *ApJ*, 628, 343
- Poisson, E. & Will, C. M. 1995, *Phys. Rev. D*, 52, 848
- Postnov, K. A. & Yungelson, L. R. 2006, *Living Reviews in Relativity*, 9, 6
- Sadowski, A., Belczynski, K., Bulik, T., et al. 2008, *ApJ*, 676, 1162
- Santamaría, L., Ohme, F., Ajith, P., et al. 2010, *Phys. Rev. D*, 82, 064016
- Schutz, B. F. 2011, *Classical and Quantum Gravity*, 28, 125023
- Shoemaker, D. for the LIGO Scientific Collaboration. 2010, *Advanced LIGO anticipated sensitivity curves*, <https://dcc.ligo.org/LIGO-T0900288/public>
- Somiya, K. 2012, *Classical and Quantum Gravity*, 29, 124007
- Strolger, L.-G., Riess, A. G., Dahlen, T., et al. 2004, *ApJ*, 613, 200
- Taylor, J. H. & Weisberg, J. M. 1989, *ApJ*, 345, 434
- Thorne, K. S. 1974, *Astrophys. J.*, 191, 507
- Virgo Collaboration. 2009, *Advanced Virgo Baseline Design*, *Virgo Technical Report VIR-0027A-09*, <https://tds.ego-gw.it/itf/tds/file.php?callFile=VIR-0027A-09.pdf>
- Voss, R. & Tauris, T. M. 2003a, *MNRAS*, 342, 1169
- . 2003b, *MNRAS*, 342, 1169
- Webbink, R. F. 1984, *ApJ*, 277, 355
- Xu, X.-J. & Li, X.-D. 2010, *ApJ*, 716, 114
- Yuan, T.-T., Kewley, L. J., & Richard, J. 2013, *ApJ*, 763, 9

APPENDIX

SINGLE AND MULTIDETECTOR RESPONSE

The “expected detection rate for GW detectors” is a theorist’s idealization. First and foremost, the event rate depends sensitively on the (time-dependent) performance of instruments in development. Furthermore, real GW searches employ complicated detection thresholds, accounting for noise non-gaussianity and non-stationarity; for multiple instruments with unequal power spectra; and for some search-dependent consistency requirement across multiple detectors. Rather than attempt realism, our idealizations provide a concrete, reproducible filter to identify the number and (critically) distribution of “detectable” binaries.

Cumulative amplitude distribution for a single detector

In a simple idealization, the detection threshold depends only on a single detector’s SNR. Several authors have characterized the response of a single GW detector to the angular distribution of power for a GW source dominated by $(l, |m|) = (2, 2)$ multipole radiation (Finn & Chernoff 1993; Finn 1996; O’Shaughnessy et al. 2010a). This response depends on the 2-dimensional sky location Ω , inclination ι , and polarization ψ , and can be conveniently summarized by a projection parameter w which is maximum ($w = 1$) for a face-on, overhead source, and minimum ($w = 0$) for sky locations and orientations where the detector has no response to the source. The SNR, $\rho(\Omega, \psi, \iota)$, is equal to the maximum SNR of a face-on, overhead source at the same distance scaled by w , i.e., $\rho = w\rho_{\text{opt}}$. The cumulative

distribution function for w is $P(w)$:

$$P(w) = \int_V \frac{d\Omega}{4\pi} \frac{d\psi}{\pi} \frac{d\cos\iota}{2} \quad (\text{A1})$$

where we integrate over the 4-dimensional angular integration volume, V , which is the set of all Ω, ι, ψ such that the response exceeds w . Our expression is identical to the cumulative distribution function $P(\Theta)$ defined by Finn & Chernoff (1993) and discussed also by Finn (1996), but we use the variable $w = \Theta/4$ such that $0 < w < 1$: (see e.g. O’Shaughnessy et al. 2010a; Belczynski et al. 2014). Note that $\langle w^2 \rangle = (2/5)^2$, therefore the optimal SNR at a given distance and the square root of the angle-averaged signal power for a source at that distance ($\rho_{\text{ave}}^2 \equiv \langle \rho^2 \rangle$) are related by $\rho_{\text{opt}} = (5/2)\rho_{\text{ave}}$. Meanwhile, $\langle w^3 \rangle^{-1/3} \simeq 2.264$ is the factor commonly used to relate volume-averaged distances to optimal detection distances, where $\langle w^3 \rangle$ is the fraction of detectable sources within a sphere whose radius equals the at-threshold detection distance for an optimally located and oriented source; see, e.g., Eq. (6) of O’Shaughnessy et al. (2010a).

Easily-interpolated tabulated results for $P(w)$ are available online³. The analytic approximation to this distribution function given by Finn (1996) is inadequate for our purposes; our tabulated results follow from sampling the distribution numerically via a Monte Carlo over 10^9 binaries. We found that a good three-parameter fit to the data is

$$P(w) = a_2^{(n)}[(1 - w/\alpha^{(n)})^2] + a_4^{(n)}[(1 - w/\alpha^{(n)})^4] + a_8^{(n)}[(1 - w/\alpha^{(n)})^8] + (1 - a_2^{(n)} - a_4^{(n)} - a_8^{(n)})[(1 - w/\alpha^{(n)})^{10}], \quad (\text{A2})$$

where (n) refers to the number of detectors in the network, $\alpha^{(n)}$ is the maximum value that w can attain, so that $\alpha^{(1)} = 1$ as w is bounded between 0 and 1, and the coefficients are $a_2^{(1)} = 0.374222$, $a_4^{(1)} = 2.04216$, and $a_8^{(1)} = -2.63948$. Notice that Eq. (A2) ensures that $P(\alpha^{(1)}) = 0$ and $P(0) = 1$.

Cumulative amplitude distribution for multiple detectors

For a multidetector network A , a network SNR ρ_A can always be defined. Following an identical procedure as above, we can define a cumulative distribution P_A that generalizes Eq. (A1). As before, $w = \rho/\rho_{\text{opt}}$, but for multidetector networks composed of instruments with equal sensitivity, ρ is the network SNR while ρ_{opt} is the single-detector SNR from an optimally-oriented binary directly overhead that detector. For three identical instruments at the LIGO Hanford, Livingston, and Virgo sites, tabulated results for P_A are available online at the URL listed in the previous footnote; a good fit to the data has the form given in Eq. (A2), but now $0 < w < 1.4$, so that $\alpha^{(3)} = 1.4$. The coefficients we obtain are $a_2^{(3)} = 1.19549$, $a_4^{(3)} = 1.61758$, and $a_8^{(3)} = -4.87024$.

Schutz (2011) described a simple idealized model for the sensitivity of multi-instrument networks. This model is almost equivalent to our own. The two models differ in that Schutz (2011), in his Eqs.(14)–(15), replaces w^2 by an (unphysical) average of w^2 over polarization, then treats the rms value of w [i.e., $\langle w^2 \rangle^{1/2}$] as a substitute for w whenever w appears. Our results adopt no such simplifying approximation.

Higher harmonics

Real GW sources produce multimodal radiation, with each mode providing a distinct angular pattern. For low-mass sources these higher harmonics contribute little to the detector’s response. For high-mass binaries with asymmetric mass ratios, higher harmonics can contribute significantly to the observationally accessible signal (Capano et al. 2013). For nonspinning binaries of total mass $M < 60M_\odot$, and with the smaller mass $> 1.2M_\odot$, we expect higher harmonics to increase the SNR ρ by less than a few percent, consistent with extrapolations derived using PN waveforms. This expectation is supported by investigations carried out with a multimodal EOB IMR waveform (Pan et al. 2011). To a good approximation, the SNR ρ and angular distribution $P(w)$ can be approximated by the corresponding expressions derived assuming purely quadrupolar, (2, 2)-mode emission.

Higher harmonics can play a significant role if the mass distribution extends to very high *redshifted* mass. At high mass, higher harmonics contribute a greater fraction of the SNR, each in a distinctive angular pattern; see O’Shaughnessy et al. (2010c) for illustrative results. For aLIGO, systematic astrophysical uncertainties such as the BH spin and mass have a significantly greater impact than the harmonic content. These higher harmonics will be important for third-generation interferometers, like the Einstein Telescope. This will be investigated in future work.

³ Data files can be found online at the following URL:

<http://www.phy.olemiss.edu/~berti/research.html>.